physica status solidi rrl
www.pss-rapid.com

Artificial Biphasic Synapses Based on Nonvolatile Phase-Change Photonic Memory Cells

*Wen Zhou, Nikolaos Farmakidis, Xuan Li, James Tan, Samarth Aggarwal, Johannes Feldmann, Frank Brückerhoff-Plückelmann, C. David Wright, Wolfram H. P. Pernice, and Harish Bhaskaran**

Nonvolatile photonic memory cells are basic building blocks for neuromorphic hardware enabling the realization of all-optical synapses and artificial neurons. These devices commonly exploit chalcogenide phase-change materials, which are evanescently coupled to photonic waveguides, and provide fast write/erase speeds and large storage capacity. Here, we report for the first time the programming of a nonvolatile photonic memory cell based on $Ag_3In_4Sb_{76}Te_{17}$ (AIST) which is capable of mimicking biphasic synapses. We evaluate the underlying mechanism of biphasic behavior of AIST cells based on numerical simulations and correlate to experimental findings. Switching dynamics demonstrate enhanced performance with a post-excitation dead time as short as 12.8 ns. Based on AIST double cells, we demonstrate reversible multilevel switching between 45 unique synaptic weights for long-term depression (LTD) and long-term potentiation (LTP). The observed biphasic programming and excellent switching performance render AIST-based photonic memory cells promising for artificial neural networks and neuromorphic photonic computing hardware.

1. Introduction

The implementation of photonic memory cells based on chalcogenide phase-change materials (PCMs) has attracted attention due to their fast, reversible, and nonvolatile programming capabilities.[1] Integrating PCM memory cells, for example, $Ge_2Sb_2Te_5$ (GST) and AgInSbTe (AIST),[2] on silicon photonic platforms enables all-optical in-memory processing with significant advantages over their electronic counterparts, in bandwidth, speed, and parallel processing.[3,4] Impressive progress has been reported in developing optical logic gates,[5,6] reconfigurable photonic circuits,[7–9] electrically controlled photonic memory cells,[10,11] plasmonic waveguide switches,[12,13] neuro-inspired photonic synapses,[14] and neural networks.[15,16] Previous studies systematically investigated the performance of photonic memory cells on silicon-nitride-on-insulator (Si_3N_4) and silicon-on-insulator (SOI) platforms,[17,18] where monotonically increased transmission was observed from the baseline (fully crystalline state) as a function of programming power. This well-established monotonic optical programming has enabled the variable plasticity resembling the spike-timing-dependent plasticity (STDP) of a basic biological neural synapse for Hebbian learning.[14] Notably, artificial synapses have been recently developed on various optoelectronic platforms,[19] for example, based on chalcogenide glass waveguides[20] and h-BN/WSe_2 heterostructure.[21] In STDP, the strength of connections between neurons, that is, synaptic weight or synaptic efficacy, is adjusted based on the relative timing of a neuron's output and input spikes. The basic formula of synaptic plasticity, that is, change in synaptic weight can be expressed as $\Delta w = f(\Delta t)$, where $\Delta t = t_{post} - t_{pre}$, t_{post}, and t_{pre} are post- and pre-neuron fire times, respectively. $\Delta t < 0$ introduces long-term depression (LTD) with $\Delta w < 0$ and $\Delta t > 0$ introduces long-term potentiation (LTP) with $\Delta w > 0$.[22]

In addition to monophasic plasticity, biphasic plasticity behavior is found in corticostriatal synapses in response to changes in dopamine concentration. Specifically, synaptic efficacy first monotonically decreases then monotonically increases to a saturated level by increasing dopamine concentration.[23,24] Previous studies suggest that biphasic behavior of the corticostriatal synapses can modulate the magnitude of Δw induced by STDP, and

W. Zhou, N. Farmakidis, X. Li, J. Tan, S. Aggarwal, J. Feldmann, H. Bhaskaran
Department of Materials
University of Oxford
Parks Road, OX1 3PH Oxford, UK
E-mail: harish.bhaskaran@materials.ox.ac.uk

F. Brückerhoff-Plückelmann, W. H. P. Pernice
Institute of Physics
University of Münster
Heisenbergstr. 11, 48149 Münster, Germany

C. David Wright
Department of Engineering
University of Exeter
Exeter EX4 4QF, UK

W. H. P. Pernice
Heidelberg University
Kirchhoff-Institute for Physics
Im Neuenheimer Feld 227, 69120 Heidelberg, Germany

The ORCID identification number(s) for the author(s) of this article can be found under https://doi.org/10.1002/pssr.202100487.

DOI: 10.1002/pssr.202100487

dopamine release may even inverse the LTP/LTD components of the normal STDP rule, that is, $\Delta t < 0$ introduces LTP with $\Delta w > 0$ and $\Delta t > 0$ introduces LTD with $\Delta w < 0$.[24] Thus, dopamine release provides a new degree of freedom for manipulating the normal STDP rule. Mimicking biphasic synapse may foster neuromorphic hardware for adaptive neural networks with improved accuracy of pattern recognition and prediction.[25]

Here, we report the first implementation of an artificial biphasic synapse on a photonic platform based on AIST photonic memory cells. AIST has been widely used in rewritable optical discs since 1993;[26,27] however, its usage in integrated photonics is arguably less studied when compared to GST.[28,29] AIST is primarily a Sb–Te binary compound with a small amount of doped In and Ag,[30] and the most common alloy is $Ag_3In_4Sb_{76}Te_{17}$, which is used in this work. Our starting state is an intermediate state with an amorphous AIST (aAIST) region in the crystalline matrix (cAIST) instead of a fully crystalline state used in previous studies.[17,18] In our all-optical pump–probe experiment, we observed a fast recrystallization process with corresponding transmission decreases and amorphization with corresponding transmission increments achieved in an AIST cell through single shot 20 ns optical write pulses. We provide the first systematic investigation of transmission of an AIST cell with respect to programming power. And we demonstrate biphasic programming by mapping the write pulse power to dopamine concentration, as well as the transmission of an AIST cell to synaptic efficacy. Then, the underlying mechanism is interpreted based on numerical simulations to estimate the thermal distributions in the spatial and temporal domains for an intermediate-state AIST waveguide memory cell. We also investigate the switching dynamics to validate recrystallization-to-amorphization transitions by simply increasing write pulse power, demonstrating a post-excitation dead time as short as 12.8 ns. We then achieve photonic biphasic plasticity on AIST double cells with 45 unique synaptic weights, significantly improving on our previous work.[28] Thus, we show that these AIST-based photonic memory cells are a promising candidate for integrated photonic synapses with biphasic plasticity and in-memory neuromorphic computing.

2. Results and Discussion

Figure 1a shows schematic of a corticostriatal synapse.[23,24] A cortical neuron releases glutamate onto the spiny neuron. Dopaminergic neuron also projects onto the spiny neuron. Especially, dopamine fluctuation influences long-term corticostriatal plasticity. Previous vivo studies suggest a biphasic corticostriatal synapse model versus the dopamine concentration, that is, low concentrations of dopamine stimuli induce depression in the region I, however, high concentrations of dopamine stimuli induce potentiation for synaptic plasticity in the region II.[23,24] Using an intermediate-state AIST photonic memory cell as shown in Figure 1b, we mimic this biphasic behavior on our photonic chip. Figure 1c shows an optical micrograph of a hot-plate annealed AIST cell on the Si_3N_4 waveguide. Specifically, our AIST memory cell is a fully etched Si_3N_4 waveguide (width = 1.2 μm, height = 0.325 μm) with a 20 nm thick AIST and a 15 nm thick indium tin oxide (ITO) stacked on top. Arrays of over 60 waveguide memory cells were fabricated

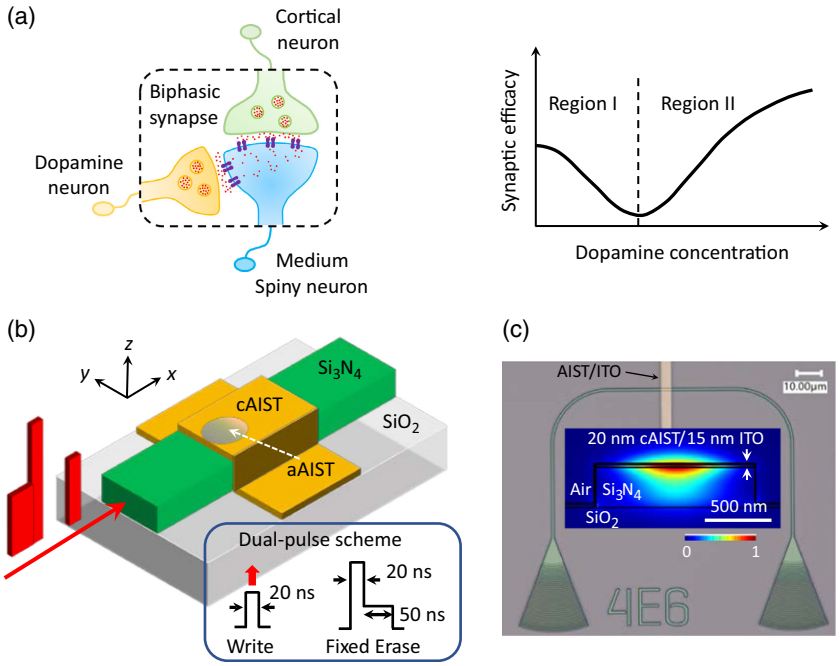

Figure 1. Biphasic synapse. a) Schematic of the corticostriatal synapse and corticostriatal biphasic synaptic efficacy versus the dopamine concentration. Induction of synaptic depression (potentiation) by increasing dopamine concentration in the region I (II). b) Schematic of an intermediate-state AgInSbTe (AIST) memory cell on a silicon nitride (Si_3N_4) waveguide to mimic biphasic synapses. Inset shows the dual-pulse scheme (20 ns write pulse of monotonically increasing power and a fixed erase pulse). c) An optical micrograph of the waveguide device. Inset shows electric field profile of the fundamental transverse-electric (TE) mode in the Si_3N_4 waveguide with coverage of cAIST/indium tin oxide (ITO) (20/15 nm) thin films.

and measured demonstrating comparable readout in the as-fabricated state. The length of AIST/ITO thin films was subsequently varied from 1 to 6 μm in steps of 1 μm to optimize the change in transmission upon optical switching. Device variation was found to be small due to using electron-beam lithography with a 10 nm resolution. The inset in Figure 1b shows the dual-pulse scheme for optical programming.[17] The inset in Figure 1c shows the $|E|$ profile of the fundamental transverse-electric (TE) mode, simulated with a 2D finite-difference time-domain (FDTD) method. To reflect the fabricated devices, coverage of AIST/ITO thin films on both sides of a waveguide are included in the simulations. Specifically, thicknesses of AIST/ITO films at waveguide sidewalls are estimated to be 2/2 nm (i.e., a 1:10 ratio of sidewall coverage in accordance to our deposition process).[31,32] At a wavelength of 1570 nm, refractive indices (n, k) of the aAIST and cAIST were measured to be (4.29, 0.20) and (6.53, 2.86) using ellipsometry, respectively. Effective refractive indices at 1570 nm are $1.76 + 0.79i$ and $2.09 + 0.02i$ for the fundamental TE modes transmitted in the Si_3N_4 waveguides with coverage of cAIST and aAIST, respectively. The waveguide mode is strongly absorbed by the 20 nm thick cAIST thin film due to a large imaginary part of effective refractive index. Confinement factor, that is, normalized integration of $|E|^2$ in the Si_3N_4 waveguide and cAIST film are 57.55% and 7.33%, respectively, while the fundamental TE mode is mainly confined in the Si_3N_4 waveguide core with aAIST. The confinement factor of $|E|^2$ in the Si_3N_4 waveguide and aAIST film are 76.36% and 3.95%, respectively (Figure S1, Supporting Information).

To achieve nonvolatile optical programming, a write–erase dual-pulse train was applied to an intermediate-state AIST memory cell along the Si_3N_4 waveguide. Our experiments were carried out based on the measurement setup detailed by Rios et al.[1] As shown in the inset of Figure 1b, the write pulse is a single-step 20 ns optical pulse with monotonically increased power from 10 to 40 mW. The erase is carried out by a fixed double-step erase pulse with pulse widths of (20, 50) ns and fixed powers of (38.13, 15.25) mW. An erase operation is done before sending every new write pulses. **Figure 2**a shows definition of transmission of an intermediate-state AIST cell. We plotted the optical transmission (T) versus write pulse power (P_{pulse}) of three intermediate-state AIST cells. These AIST cells have different initial amorphous-to-crystalline ratios, and their initial transmissions are at 9.1%, 6.8%, and 5.1% as shown in Figure 2b–d, respectively. By simply increasing write pulse power, we observed first decreasing and then increasing of transmission in the regions I and II, respectively. Turning points are at 16.1, 15.7, and 16.3 mW for these three cells, with repeatability in nonvolatile optical programming. To mimic a biological biphasic synapse, the write pulse power is mapped to the dopamine concentration and the transmission is mapped to the synaptic efficacy. Thus, our nonvolatile programming directly mimics the corticostriatal synapses in response to the dopamine concentration as shown in Figure 1a.

To interpret the underlying mechanism, we next numerically investigated the thermal distributions in an intermediate-state AIST cell by performing 3D FDTD and finite-element method (FEM) simulations. An AIST memory cell as shown in **Figure 3**a was characterized by optical microscopy and scanning electron microscopy (SEM). With this cell, we observed the

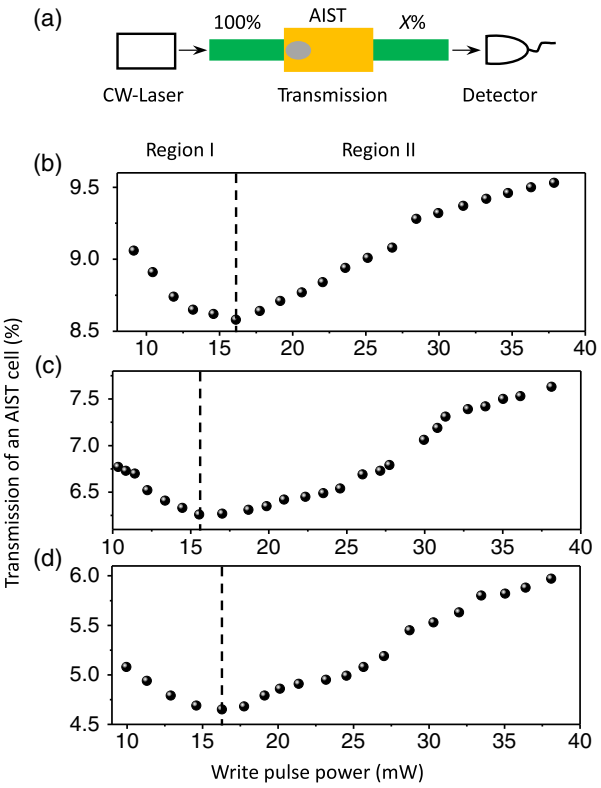

Figure 2. Mimicking biphasic response. a) Definition of transmission ($T = X\%$) of an intermediate-state AIST cell. b–d) Transmission versus write pulse power for pulses with a length of 20 ns for three 5 μm long intermediate-state AIST cells with different initial amorphous-to-crystalline ratios; initial transmissions are b) 9.1%, c) 6.8%, and d) 5.1%. Dashed line is the boundary between regions I and II.

nonvolatile and biphasic programming. Based on SEM imaging, an elliptical area (measured radii = 520 and 410 nm) was considered as the aAIST region within the crystalline matrix (cAIST), and simplified as an intermediate-state AIST cell for our simulation model. Based on the dual-pulse programming, the last pulse we sent was a fixed erase pulse. Thus, the observed intermediate state in Figure 3a was treated as an erased state for each injected write pulse with monotonically increased power.

In numerical simulations, FDTD method first solves a unit power absorption (P_{abs}) profile for this AIST cell (Figure S2, Supporting Information), and P_{abs} was next imported into the FEM solver as a local heat source to obtain the spatial and transient temperature profiles. Material properties used in the FEM simulations can be found in Table S1, Supporting Information. Figure 3b shows spatial temperature profiles at the AIST − ITO thin-film interface generated at the write pulse falling edge (time = 20 ns in Figure 3c) heated by 20 ns write pulses at 10, 15.7, 20, and 30 mW. Note that color scale is saturated at the melting temperature of 817 K.

Specifically, when power is 15.7 mW, generated peak temperature is 729.7 K, which is lower than the melting temperature T_m of 817 K and the phase transition from cAIST to aAIST is forbidden. In this case, a single shot of low-power 20 ns write pulse enables recrystallization from the amorphous–crystalline

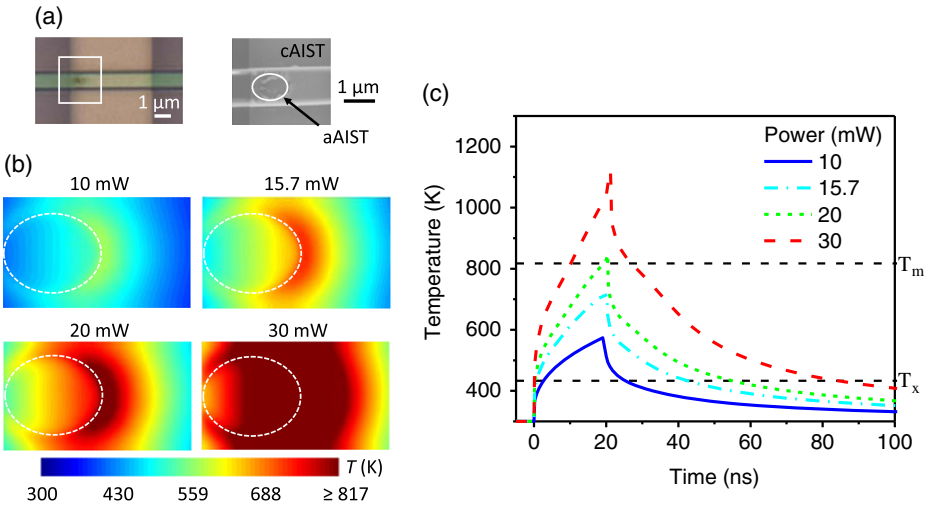

Figure 3. Numerical investigation of the biphasic mechanism. a) Optical micrograph and scanning electron microscopic (SEM) images of an intermediate-state AIST cell programmed by an erase pulse. b) Spatial temperature profiles of the AIST cell ($2 \times 1.2\ \mu m^2$) generated at the pulse falling edge (time = 20 ns) after sending 20 ns write pulses with powers of 10, 15.7, 20, and 30 mW. Rising and falling of write pulses are at time = 0 and 20 ns, respectively. c) Transient profiles of the peak temperature in the same AIST cell upon sending the write pulses as in (b).

(aAIST–cAIST) rim because its temperature is between transition temperature T_x (=433 K) and melting temperature T_m.[28] On the other hand, an Arrhenius behavior was observed for the crystal growth velocity as a function of temperature in the melt-quenched aAIST.[33] By comparing temperature profiles generated at 10 and 15.7 mW in Figure 3b, increased crystal growth velocity results from overall increased temperature at the aAIST–cAIST rim. Figure 3c shows peak temperature evolution in the time domain for the same intermediate-state AIST cell upon sending the 20 ns write pulses with powers of 10, 15.7, 20, and 30 mW. It is also observed that the state has a much longer time duration of 43.2 ns above T_x at 15.7 mW than 22.1 ns at 10 mW. Therefore, a larger area of aAIST within the white ellipse can be recrystallized from aAIST–cAIST rim due to integrating a higher crystal growth velocity over a longer time duration above T_x. This leads to decremental transmission by increasing write pulse power in the region I.

By further increasing the write power, melt-quenching takes place in the dark red area with temperature exceeding T_m in Figure 3b. By comparing temperature profiles generated at 30 and 20 mW in Figure 3b, a growing area outside aAIST–cAIST rim with temperature exceeding T_m can be amorphized. This leads to incremental transmission by increasing write pulse power in the region II. The same explanation for incremental transmission in a GST cell can be found in a previous study.[17] However, in the AIST cell, accompanying fast recrystallization may also happen in the temperature rising and falling processes with temperature between T_x and T_m. Figure 2c shows that total time durations are respectively 52.2 and 68.1 ns when temperature is between T_x and T_m at 20 and 30 mW. As deduced from Figure 2b–d, in the region II, amorphization first compensates the accompanying recrystallization with transmission still less than the initial value, then amorphization dominates with transmission higher than the initial value by further increasing the write pulse power.

With the same device, we also investigated the switching dynamics in the regions I and II. Specifically, the AIST cell was excited by a 20 ns write pulse with a power of 15.43 mW and an erase pulse with pulse widths of (20, 50) ns and powers of (38.08, 14.80) mW. As shown in **Figure 4**a, upon sending optical pulses, the normalized transmission drops due to thermo-optical effect.[1] Working at region I, a low-power write pulse leads to a decrease in normalized transmission of probe light to around −0.4 after reaching equilibrium indicated by a red dotted arrow pointing downward, which validates that the low-power write pulse is basically a recrystallization pulse. The probe transmission was erased back to 0 after sending an erase pulse. The post-excitation dead times were measured to be 19.2 and 36.8 ns, respectively. Therefore, total time consuming required for settling and erasing are 39.2 and 106.8 ns, respectively. As shown in Figure 4b, working at region II, normalized transmission of probe light first increases to 0.33 after sending a high-power write pulse, and was subsequently erased to 0. The post-excitation dead times were measured to be 12.8 and 44.8 ns, respectively. The total times required for settling and erasing are 32.8 and 114.8 ns, respectively. Switching dynamics in Figure 4 validate recrystallization-to-amorphization transition by simply increasing write pulse power. The retention timescale of LTDs and LTPs will depend on the temperature of the AIST cell and can persist for hours at room temperature.[3,28] No recrystallization is observed after weight updating in our experiments when setting the probe power to sufficiently low values (0.36 mW) for continuous-wave (CW) probing in the waveguide.[34] Using this power level, a nearly constant readout is monitored, wherein this synaptic weight can in principle persist for years at room temperature using nonvolatile AIST memory cells.[35]

Having discussed the switching dynamics, we next describe multilevel operation of the biphasic synapse. **Figure 5**a shows a schematic of a biphasic synapse that consists of 3 μm long

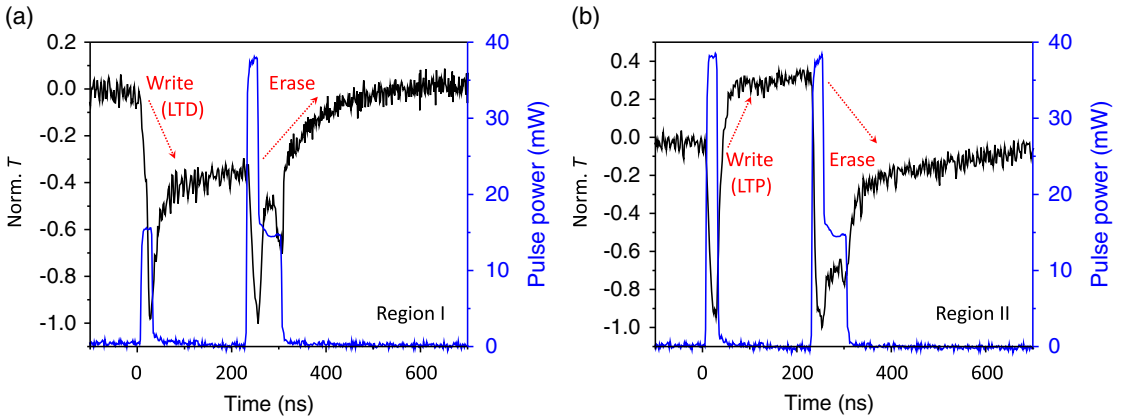

Figure 4. Switching dynamics in the regions I and II. a,b) Measured optical powers of the write and erase pulses (blue curves) in the waveguide before the AIST cell and normalized time-dependent transmission of the probe light (black curves) operated in the region I (a) and the region II (b). Red dotted arrows indicate switching events upon sending the write and erase pulses. Norm. T is calculated by $(T - T_{Erase})/(T_{Erase} - T_{min})$, where T_{Erase} is the transmission of an erased state and T_{min} is the recorded minimal transmission due to thermal-optic effect.

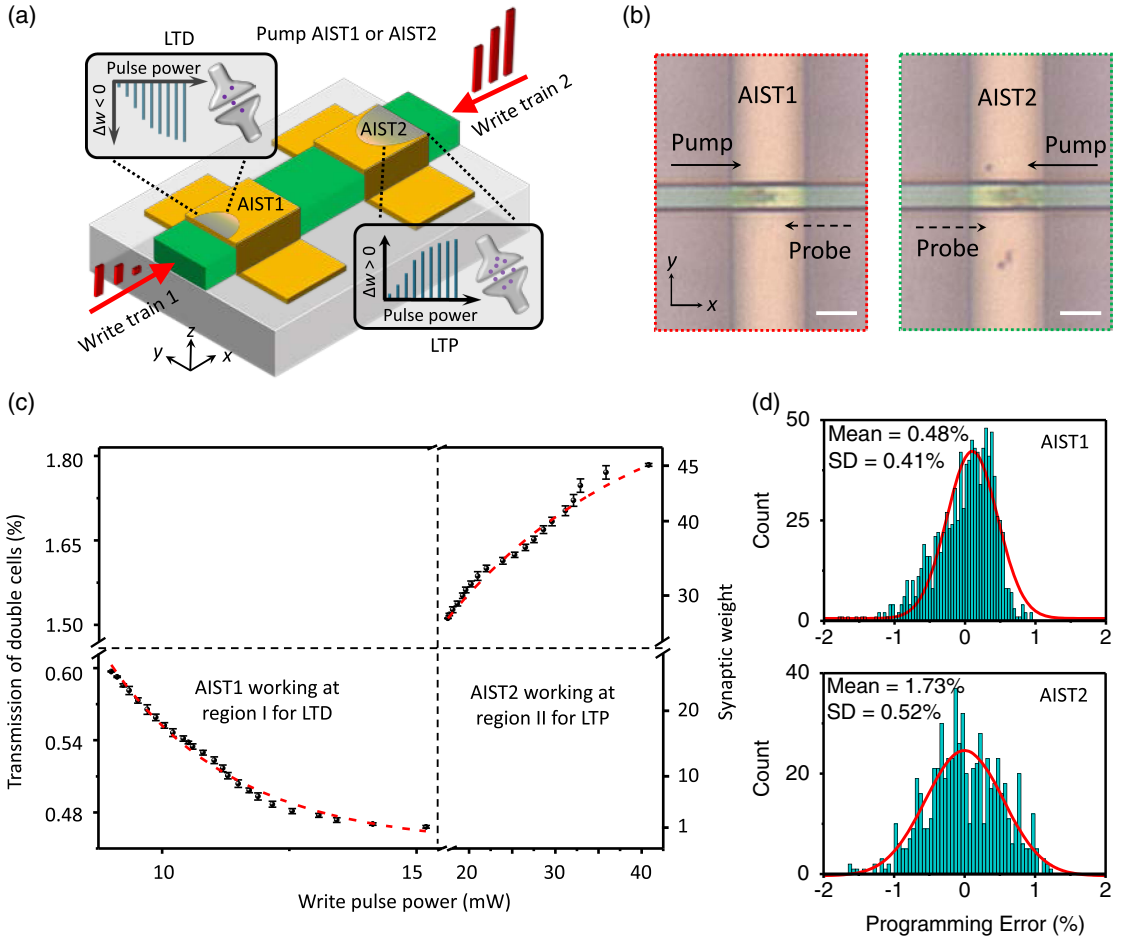

Figure 5. Multilevel operation of a photonic biphasic synapse. a) Schematic of the integrated photonic synapse, which consists of AIST double cells (AIST1 and AIST2) on a Si_3N_4 waveguide. b) Optical micrographs of the AIST double cells. The scale bars show 2 μm. c) Transmission of AIST double cells as a function of write pulse power. It has the same transmission definition as that in Figure 2a. Black bars and red dashed curves respectively denote standard deviation and exponential fitting of the transmission. Forty-five unique synaptic weights (25 weights in the region I for long-term depression [LTD] and 20 weights in the region II for long-term potentiation [LTP]) can be resolved. d) Histograms of programming errors.

AIST double cells on a Si_3N_4 waveguide. To update the synaptic weight, either AIST cell 1 working at region I or AIST cell 2 working at region II is programmed with a single 20 ns recrystallization or amorphization write pulse to achieve LTD or LTP plasticity. Figure 5b shows optical micrographs of the AIST cell 1 and AIST cell 2 after multilevel programming. AIST cell 1(2) was pumped along $x(-x)$ direction and was probed along $-x(x)$ direction. Write pulse with a pulse width of 20 ns and monotonically increased power of 9.0–15.2 mW encodes an arbitrary synaptic weight with a reduced transmission for the AIST cell 1 to mimic LTD. Next, to program the AIST cell 2, only pump and probe directions were swapped while pump and probe wavelengths were still fixed as 1570.4 and 1575.4 nm, respectively. With the same pulse widths, the AIST cell 2 working at region II was programmed with increased power of 18.7–41.0 mW for the write pulses. High-power write pulses melt-quenched the AIST cell 2, which was set with a larger aAIST-to-cAIST ratio and a higher transmission relative to the previous value to mimic LTP. Note that a 2.22 nJ erase pulse defines a baseline with a transmission of 1.5% in the LTP regime, which is higher than the baseline (0.6%) in the LTD regime defined by a 1.47 nJ erase pulse. Therefore, there is no overlap between these discrete synaptic weights in the LTD and LTP regimes. AIST cell 1 and cell 2 were respectively programmed by nine iterations with the aforementioned same pulse parameters, and their transmissions for each synaptic weight were recorded. Standard deviation was calculated for the error between the averaged transmission and actual transmission for each weight. Forty-five distinct synaptic weights with no overlap in standard deviation can be resolved as shown in Figure 5c. Dependence of the synaptic weight change, that is, synaptic plasticity ($\Delta w = \Delta T = (T - T_{\text{baseline}})/T_{\text{baseline}} \times 100\%$) on the write pulse power (P_{pulse}) was fitted by $\Delta w = -\Delta w_0 + Ae^{-P\text{pulse}/\tau}$ in the region I for LTD and $\Delta w = \Delta w_0 - Ae^{-P\text{pulse}/\tau}$ in the region II for LTP, shown as the red dashed curves in Figure 5c. T and T_{baseline} are transmission and baseline of AIST double cells. Detailed fitting parameters can be found in Table S2, Supporting Information. Figure 5d plots histograms of the programming error for the AIST cell 1(2) with averaged transmission of 0.48% (1.73%) and standard deviations of 0.41% (0.52%) for the synaptic weight "5" ("42"). This allows robust and arbitrary tailoring of the synaptic weight to mimic the biological biphasic synapses.

3. Conclusion

We have proposed and experimentally demonstrated an integrated photonic biphasic synapse based on an intermediate-state AIST photonic memory cell for the first time. We observe two distinct regions where biphasic response results from fast recrystallization in region I and competition between amorphization and accompanying recrystallization processes in region II. Investigation on the switching dynamics shows post-excitation dead times of 12.8–44.8 ns. Low- and high-power 20 ns write pulses respectively initiate fast recrystallization for LTD ($\Delta w < 0$) and amorphization for LTP ($\Delta w > 0$) for AIST photonic memory cells. Multilevel operation with 45 synaptic weights can be reliably accessed. Rapid recrystallization and amorphization can also be readily achievable by using picosecond optical pulses to further reduce energy consumption and to enhance programming speed of waveguide memories.[28] This study enabled us to design a flexible biphasic programming technique using nonvolatile and multilevel photonic memories with low programming error. It is crucial for practical memory applications due to leveraging large bandwidth and ultrafast optical signaling. It may also pave the way for programming artificial synapses initialized with random and weak connection strengths in the neural networks, which can be trained efficiently by the stochastic optimization algorithm.[36] For future work, these artificial biphasic synapses may be wired to an integrate-and-fire neuron for unsupervised learning, and can be scalable as a deep neural network based on wavelength division multiplexing architectures for high-density neuromorphic hardware applications.[15]

4. Experimental Section

Device Fabrication: Low-pressure chemical vapor deposition (LPCVD) Si_3N_4 on insulator wafers (Si_3N_4 device layer thickness = 325 nm) (Rogue Valley Microdevices) was patterned by a Raith EBPG 5150 electron-beam lithography (ebeam) to form the etch mask in the spin-coated negative-tone ebeam resist arN 7520.12 after development in MF-319. CHF_3/O_2-based reactive ion etching was carried out to fully etch the Si_3N_4 device layer and form photonic integrated circuits with a waveguide width of 1.2 μm and a height of 325 nm. In a second step of ebeam, sputtering windows for AIST cells were exposed in the bilayer positive tone resist polymethylmethacrylat (PMMA 495 A8 and 950 A8) after development in isopropyl alcohol:methyl isobutyl ketone:ethyl methyl ketone (15:5:1). A stack of 20 nm AIST with a 15 nm ITO-protective capping was deposited in an argon environment using a radio frequency sputtering system (Nordiko). After sputtering, the bilayer PMMA was lifted off in acetone, leaving patterned PCM cells on the Si_3N_4 photonic circuitry. Prior to the experiments, AIST cells were annealed on a hot plate at 250 °C for 10 min.

Measurement Setup: Two CW diode lasers (N7711A, Keysight Technologies) with different wavelengths (1570.4 nm for pump and 1575.4 nm for probe) and power of 3.55 mW were used in the all-optical pump–probe experiment. To generate nanosecond write and erase pulses, the pump laser beam first passed through a fiber polarization controller (FPC032, Thorlabs), and was next modulated by an electro-optic modulator driven by an arbitrary function generator (Tektronics 100 MHz AFG3102C) with dual output channels to separately send out write and erase pulses. An electronic variable optical attenuator (VOA) (THORLABS V1550) was programmed to control the write pulse power for biphasic programming. Pump pulse power was further amplified by an erbium-doped fiber amplifier (EDFA) (AEDFA-CL-23, Amonics Ltd.). Pump and probe were coupled into the Si_3N_4 photonic integrated circuits from different input ports based on the apodized grating couplers with optimized transmission using FPCs, such that pump and probe transmitted along the opposite directions through the AIST photonic memory cells. Noises from pump reflection were filtered by an optical band-pass filter (optical tunable filter-320, Santec) for the probe detection. A 200 kHz low-noise photoreceiver (2011-FC, Newport) was used to record dynamic change of the probe transmission. The thermo-optical response was measured with a 1 GHz photoreceiver (1611FS-AC, Newport) and a fast-sampling oscilloscope (TDS7404, Tektronix, Inc.).

Supporting Information

Supporting Information is available from the Wiley Online Library or from the author.

Acknowledgements

The authors acknowledge funding for this work from the European Union's Horizon 2020 Research and Innovation Program (Fun-COMP project, #780848).

Conflict of Interest

The authors declare no conflict of interest.

Data Availability Statement

The data that support the findings of this study are available from the corresponding author upon reasonable request.

Keywords

artificial synapses, neuromorphic photonics, nonvolatile photonic memory, phase-change materials

Received: September 12, 2021
Revised: March 7, 2022
Published online: April 27, 2022

[1] C. Rios, M. Stegmaier, P. Hosseini, D. Wang, T. Scherer, C. D. Wright, H. Bhaskaran, W. H. P. Pernice, *Nat. Photonics* **2015**, *9*, 725.
[2] W. Zhang, R. Mazzarello, M. Wuttig, E. Ma, *Nat. Rev. Mater.* **2019**, *4*, 150.
[3] C. Rios, N. Youngblood, Z. Cheng, M. Le Gallo, W. H. P. Pernice, C. D. Wright, A. Sebastian, H. Bhaskaran, *Sci. Adv.* **2019**, *5*, eaau5759.
[4] J. Feldmann, N. Youngblood, M. Karpov, H. Gehring, X. Li, M. Stappers, M. L. Gallo, X. Fu, A. Lukashchuk, A. Raja, J. Liu, D. Wright, A. Sebastian, T. Kippenberg, W. Pernice, H. Bhaskaran, *Nature* **2021**, *589*, 52.
[5] Z. Cheng, C. Rios, N. Youngblood, C. D. Wright, W. H. P. Pernice, H. Bhaskaran, *Adv. Mater.* **2018**, *30*, 1802435.
[6] R. R. Ghosh, A. Dhawan, *Sci. Rep.* **2021**, *11*, 18811.
[7] P. Xu, J. Zheng, J. K. Doylend, A. Majumdar, *ACS Photonics* **2019**, *6*, 553.
[8] C. Wu, H. Yu, H. Li, X. Zhang, I. Takeuchi, M. Li, *ACS Photonics* **2019**, *6*, 87.
[9] H. Hu, H. Zhang, L. Zhou, J. Xu, L. Lu, J. Chen, B. M. A. Rahman, *Opt. Express* **2020**, *28*, 1574.
[10] H. Zhang, L. Zhou, L. Lu, J. Xu, N. Wang, H. Hu, B. M. A. Rahman, Z. Zhou, J. Chen, *ACS Photonics* **2019**, *6*, 2205.
[11] J. Zheng, Z. Fang, C. Wu, S. Zhu, P. Xu, J. K. Doylend, S. Deshmukh, E. Pop, S. Dunham, M. Li, A. Majumdar, *Adv. Mater.* **2020**, *32*, 2001218.
[12] M. Rudé, R. E. Simpson, R. Quidant, V. Pruneri, J. Renger, *ACS Photonics* **2015**, *2*, 669.
[13] N. Farmakidis, N. Youngblood, X. Li, J. Tan, J. L. Swett, Z. Cheng, C. D. Wright, W. H. P. Pernice, H. Bhaskaran, *Sci. Adv.* **2019**, *5*, eaaw2687.
[14] Z. Cheng, C. Rios, W. H. P. Pernice, C. D. Wright, H. Bhaskaran, *Sci. Adv.* **2017**, *3*, 1700160.
[15] J. Feldmann, N. Youngblood, C. D. Wright, H. Bhaskaran, W. H. P. Pernice, *Nature* **2019**, *569*, 208.
[16] B. J. Shastri, A. N. Tait, T. F. D. Lima, W. H. P. Pernice, H. Bhaskaran, C. D. Wright, P. R. Prucnal, *Nat. Photonics* **2021**, *15*, 102.
[17] X. Li, N. Youngblood, C. Rios, Z. Cheng, C. D. Wright, W. H. P. Pernice, H. Bhaskaran, *Optica* **2019**, *6*, 1.
[18] X. Li, N. Youngblood, Z. Cheng, S. Carrillo, E. Gemo, W. H. P. Pernice, C. D. Wright, H. Bhaskaran, *Optica* **2020**, *7*, 218.
[19] S. W. Cho, S. M. Kwon, Y.-H. Kim, S. K. Park, *Adv. Intell. Syst.* **2021**, *3*, 2000162.
[20] M. Ramos, V. Bharadwaj, B. Sotillo, B. Gholipour, A. N. Giakoumaki, R. Ramponi, S. M. Eaton, C. Soci, *Appl. Phys. Lett.* **2021**, *119*, 031104.
[21] S. Seo, S.-H. Jo, S. Kim, J. Shim, S. Oh, J.-H. Kim, K. Heo, J.-W. Choi, C. Choi, S. Oh, D. Kuzum, H.-S. P. Wong, J.-H. Park, *Nat. Commun.* **2018**, *9*, 5106.
[22] S. Song, K. D. Miller, L. F. Abbott, *Nat. Neurosci.* **2000**, *3*, 919.
[23] J. N. J. Reynolds, J. R. Wickens, *Neural Networks* **2002**, *15*, 507.
[24] J.-P. Thivierge, F. Rivest, O. Monchi, *Synapse* **2007**, *61*, 375.
[25] L. Wu, Z. Wang, B. Wang, Q. Chen, L. Bao, Z. Yu, Y. Yang, Y. Ling, Y. Qian, K. Tang, Y. Cai, R. Huang, *Nanoscale* **2021**, *13*, 3483.
[26] H. Iwasaki, Y. Ide, M. Harigaya, Y. Kageyama, I. Fujimura, *Jpn. J. Appl. Phys.* **1992**, *31*, 461.
[27] H. Iwasaki, M. Harigaya, O. Nonoyama, Y. Kageyama, M. Takahashi, K. Yamada, H. Deguchi, Y. Ide, *Jpn. J. Appl. Phys.* **1993**, *32*, 5241.
[28] J. Feldmann, M. Stegmaier, N. Gruhler, C. Rios, H. Bhaskaran, C. D. Wright, W. H. P. Pernice, *Nat. Commun.* **2017**, *8*, 1.
[29] C. Ríos, P. Hosseini, R. A. Taylor, H. Bhaskaran, *Adv. Mater.* **2016**, *28*, 4720.
[30] T. Matsunaga, J. Akola, S. Kohara, T. Honma, K. Kobayashi, E. Ikenaga, R. O. Jones, N. Yamada, M. Takata, R. Kojima, *Nat. Mater.* **2011**, *10*, 129.
[31] A. Sidhwa, C. Spinner, T. Gandy, M. Goulding, W. Brown, H. Naseem, R. Ulrich, S. Ang, S. Charlton, V. Prasad, T. Cale, *IEEE Trans. Semicond. Manuf.* **2005**, *18*, 163.
[32] T. Karabacak, T.-M. Lu, *J. Appl. Phys.* **2005**, *97*, 124504.
[33] M. Salinga, E. Carria, A. Kaldenbach, M. Bornhofft, J. Benke, J. Mayer, M. Wuttig, *Nat. Commun.* **2013**, *4*, 2371.
[34] N. Youngblood, C. Ríos, E. Gemo, J. Feldmann, Z. Cheng, A. Baldycheva, W. H. Pernice, C. D. Wright, H. Bhaskaran, *Adv. Funct. Mater.* **2019**, *29*, 1807571.
[35] M. Wuttig, N. Yamada, *Nat. Mater.* **2007**, *6*, 824.
[36] L. Hamm, B. Brorsen, M. Hagan, *Neural Process. Lett.* **2007**, *26*, 145.